Carbon 165 (2020) 286–295

Contents lists available at ScienceDirect

Carbon

journal homepage: www.elsevier.com/locate/carbon

Energetic metal-organic frameworks deflagration enabled ultrafast low-temperature synthesis of ultra-light magnetic nanoparticles decorated high-lossy materials

Yousong Liu [a], Bin Quan [c], Xiaohui Liang [c], Bing Huang [a], Shiliang Huang [a], Xiaodong Li [a], Guangbin Ji [c], Zhong Jin [b, **], Guangcheng Yang [a, *]

[a] Institute of Chemical Materials, China Academy of Engineering Physics, Mianyang, Sichuan, 621900, PR China
[b] Key Laboratory of Mesoscopic Chemistry of MOE, Jiangsu Key Laboratory of Advanced Organic Materials, School of Chemistry and Chemical Engineering, Nanjing University, Nanjing, 210023, PR China
[c] College of Material Science and Technology, Nanjing University of Aeronautics and Astronautics, Nanjing, 210016, PR China

ARTICLE INFO

Article history:
Received 1 December 2019
Received in revised form
20 April 2020
Accepted 25 April 2020
Available online 28 April 2020

Keywords:
Energetic metal-organic frameworks
Deflagration methodology
Ultrafast low-temperature synthesis
Electromagnetic wave absorption

ABSTRACT

Magnetic/dielectric nanocomposites featuring strong electromagnetic wave response are ideal materials for microwave absorbing, due to their high dissipation capability and optimized impedance matching. However, it is still a challenge to synthesize such nanocomposites due to the drawbacks of conventional fabrication approaches, such as considerable time consumption, high-power dissipation, low efficiency as well as insufficient contact. Here, an ultrafast energetic metal-organic framework (EMOF) deflagration methodology was proposed to transform EMOF nanoparticles to magnetic nanoparticles and simultaneously convert graphene oxide to reduced graphene oxide (RGO) by utilizing the huge heat release via one-step pyrolysis. The obtained absorbers exhibit remarkable microwave response capability at an ultra-low loading content, which verifies the practicability and advantages of this synthetic approach. Moreover, this work opens up potential opportunities for EMOFs applications in a wide range and expands the future materials design scopes.

1. Introduction

With the wide usage of electronic equipment and communication facilities in recent years, electromagnetic (EM) wave absorption materials are attracting considerable interests owing to their unique properties in solving electromagnetic pollution and interference problems [1–5]. As is known, features such as strong absorption, wide frequency band, thin thickness, light weight and high thermal stability are required for the high-performance EM microwave absorption materials [6–10]. Among all the frequently-reported stuffs, magnetic/dielectric nanocomposites are the most promising materials for microwave absorption due to their high dissipation capability and optimized impedance matching [11].

So far, many preparation methods such as solvothermal method [12–17], thermal annealing [18–24], polymerization method [25], wet chemical synthesis [9], chemical vapor deposition [26], atomic layer deposition [27] have been developed to prepare various magnetic/dielectric nanocomposites. However, some of these strategies may suffer from considerable time consumption, high-power dissipation or low efficiency. Therefore, searching novel methods for fabricating magnetic/dielectric nanocomposites with desired microstructures and excellent wave absorption properties is still a mainstream and yet remains a great challenge.

Recently, our group proposed an energetic-materials-derived-advanced-materials (EM-to-AM) synthesis strategy, which is based on the deflagration/explosion behavior of energetic materials to provide abundant highly active radicals and high temperature/pressure environment for elemental/impurities doping, micro-pore/pits forming, quantum dots or hollow nanostructures preparation and so on [28]. For example, gram-scale graphene quantum dots can be obtained via the deflagration reaction of polytetrafluoroethylene (PTFE) and Si. It's found that the high temperature and rapid temperature decrease of deflagration flame limit the carbon atoms growing into graphene quantum dots [29]. N and Ti^{3+} co-doped TiO_2 with rough surfaces and in-plane holes can be obtained from NaN_3 deflagration treatment in seconds by N radicals filling into the

* Corresponding author.
** Corresponding author.
E-mail addresses: zhongjin@nju.edu.cn (Z. Jin), ygcheng@caep.cn (G. Yang).

https://doi.org/10.1016/j.carbon.2020.04.089
0008-6223/

crystal lattices and Na clusters capturing partial O from TiO_2 [30]. Also, carbon hollow nanospheres with high N/F co-doping and high graphitization degree can be easily achieved from NaN_3/C_5F_5N deflagration based on the Na nanoclusters capturing partial F atoms from C_5F_5N and serving as sacrificial templates for the formation of hollow structures, and the heat release generating an extremely high temperature for graphitic structure formation [31]. Even single-atoms decorated porous carbon networks can be fabricated via a simple energetic metal-organic framework (EMOF) thermal transformation process [32]. In brief, the EM-to-AM strategy provides a facile and efficient approach to fabricate a series of advanced functional materials and is expected to applicated in the synthesis of microwave absorption materials.

Here, we utilize the typical Fe_3O_4/RGO nanocomposites as an example to demonstrate the feasibility for exploiting EM-to-AM strategy to fabricate high-efficiency microwave absorbers. Fe-based EMOFs ($[Fe(BTO)(H_2O)_2]_n$) and GO were employed as deflagration precursors. Once initiated, the energetic bistetrazole ligands decompose and release a huge amount of gases/heat, leading to the local reduction of GO, while Fe cations are transformed into ultra-small Fe_3O_4 nanoparticles. The obtained Fe_3O_4/RGO absorbers exhibit excellent EM wave absorption capability at an ultra-low loading content (5 wt% sample addition), which validate the practicability of as-mentioned strategy. Moreover, this EMOFs deflagration method can also be readily utilized for other advanced materials preparation, providing new insights for future materials design.

2. Results and discussion

The low-temperature deflagration preparation procedure of Fe_3O_4/RGO is shown in Fig. 1. Firstly, a certain amount of $FeSO_4$ was dissolved in 200 mL GO solution under stirring for 15 min to complete the adsorption of Fe^{2+} on GO via electrostatic interaction as GO is negative charged due to its abundant ionizable oxygen groups (Figure S1, supporting information). Then, $[Fe(BTO)(H_2O)_2]_n$/GO precursor was obtained by adding H_2BTO into the above solution by dropwise. The dried precursor was heated up to 220 °C at N_2 atmosphere to trigger the deflagration of $[Fe(BTO)(H_2O)_2]_n$. Fe-contained radicals were generated in the deflagration process and finally transformed into Fe_3O_4 nanoparticles; while the rest C-, N-and H-contained radicals transformed into CO_2, N_2O and H_2O gases. It should be noted that the deflagration-induced spray behavior of the radicals resulted in the formation of ultra-small Fe_3O_4 nanoparticles. Moreover, the huge heat release in the deflagration process generated a local high-temperature environment, which led to the removal of oxygen function groups and improvement of the electric conductivity of GO.

The reaction of $FeSO_4$ and H_2BTO produced a ribbon-shaped bis-tetrazole-based EMOF ($[Fe(BTO)(H_2O)_2]_n$, monoclinic space group $P2_1/c$), in which Fe(II) ion is hexa-coordinated by two nitrogen atoms and four oxygen atoms in a stretched octahedron as shown in Fig. 2a. Two nitrogen/oxygen atoms from two BTO^{2-} and two oxygen atoms from H_2O are located in the axial position and equatorial plane, respectively. It can be indicated from the well matched powder X-ray diffraction (PXRD) results of the as-prepared $[Fe(BTO)(H_2O)_2]_n$ with the simulated patterns that the synthesized $[Fe(BTO)(H_2O)_2]_n$ is phase-pure with high crystallinity (Fig. 2b). The SEM images in Fig. 2c and d illustrate that the ribbon-shaped $[Fe(BTO)(H_2O)_2]_n$ presents homogeneous crystals with 1–2 μm in length, 200–500 nm in width and ca. 20 nm in thickness.

When GO was added into the reaction system of $FeSO_4$ and H_2BTO, $[Fe(BTO)(H_2O)_2]_n$/GO nanocomposites were obtained, in which the $[Fe(BTO)(H_2O)_2]_n$ nanoribbons were dispersed homogeneously on the GO nanosheets, as shown in Fig. 3a and b and Figure S2. The nanoribbons decorated on the GO nanosheets exhibited reduced size with a length of less than 400 nm and a width of ca. 100 nm. It may be resulted from the steric effect of GO, which minished the EMOFs growth rate via hindering the effective mass (Fe^{2+} and BTO^{2-} species) transport. The $[Fe(BTO)(H_2O)_2]_n$/GO deflagration features and pyrolysis process are investigated by a series of characterization techniques. The TG/DSC curves in Fig. 3c show that $[Fe(BTO)(H_2O)_2]_n$ deflagration at 208 °C and lost more than 50 wt% of the whole weight accompanied with the release of CO_2, N_2O and H_2O, which are the only three final gaseous products of the BTO ligand deflagration and the subsequent GO reduction (Fig. 3d). It should be noted that the presence of GO promotes thermal decomposition of $[Fe(BTO)(H_2O)_2]_n$, which is supported by the shift of its deflagration peak in the derivative thermogravimetric analysis curve from 212 °C for $[Fe(BTO)(H_2O)_2]_n$ to 208 °C for $[Fe(BTO)(H_2O)_2]_n$/GO (Figure S3).

To clarify the heat liberation induced temperature variation in the deflagration process, infrared temperature measurement was adopted. From Fig. 3e, it can be seen that many sparks of fire distributed uniformly, indicating a homogeneous Fe_3O_4 growth and GO reduction environment. From the time-dependent temperature curve in Fig. 3f, it can be observed that the deflagration temperature was as high as ca. 720 °C and maintained for just few seconds. Note that the high temperature could promote the decomposition of oxygen-containing function groups to achieve the thermal reduction of GO, while the short duration of high temperature protects GO against completely decomposition by oxygen from air.

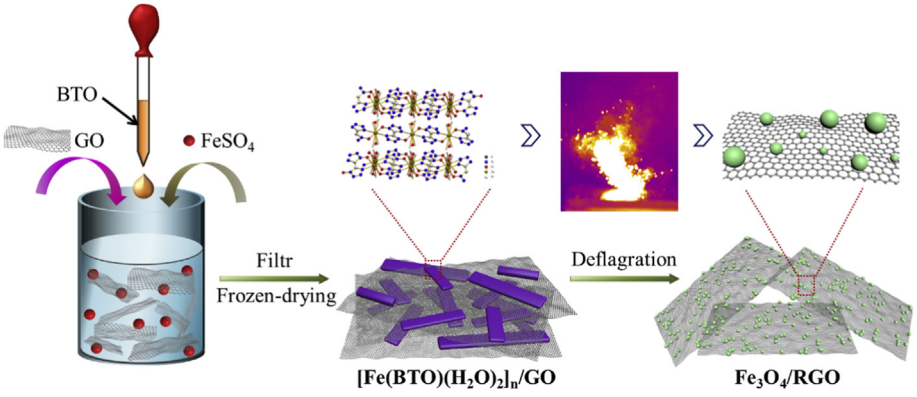

Fig. 1. Scheme diagram of the synthesis of Fe_3O_4/RGO. (A colour version of this figure can be viewed online.)

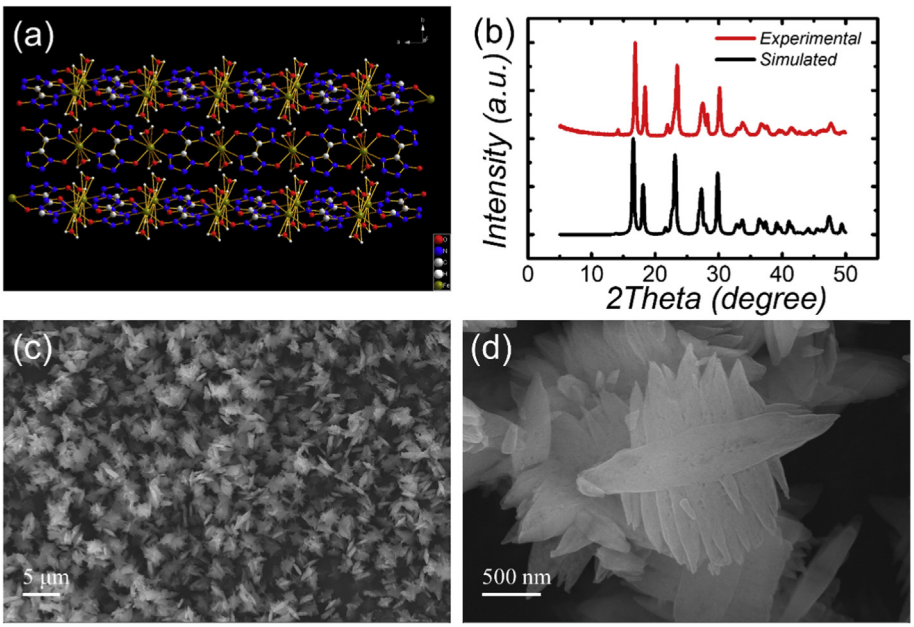

Fig. 2. a) Crystal structure, b) experimental and simulated XRD patterns and c-d) SEM images of $[Fe(BTO)(H_2O)_2]_n$. (A colour version of this figure can be viewed online.)

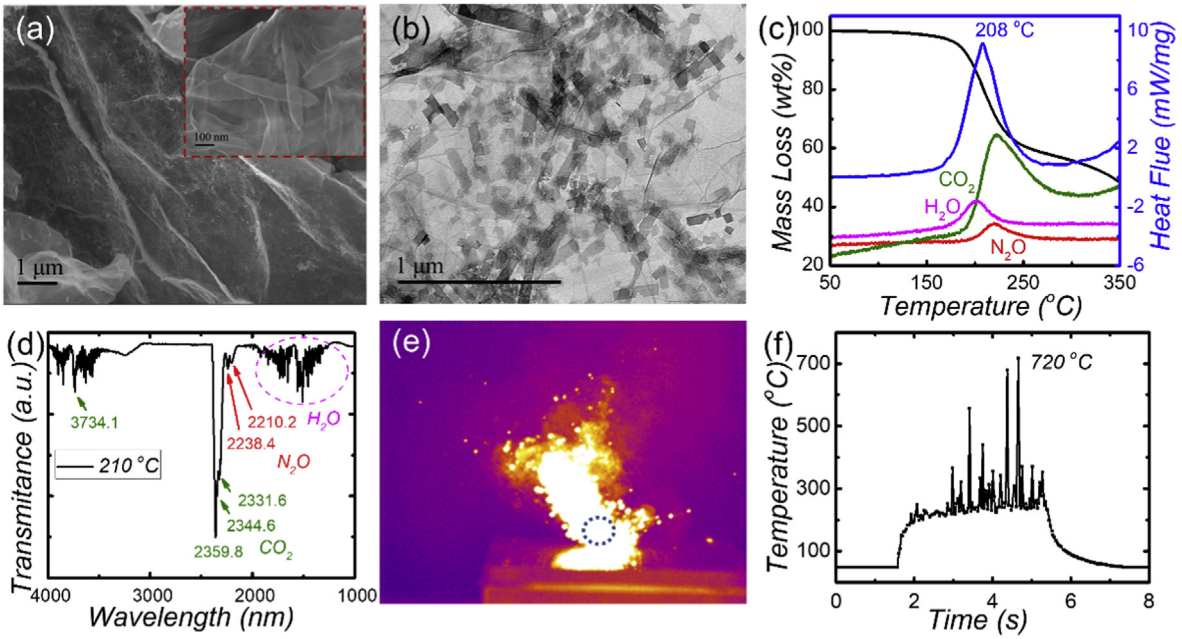

Fig. 3. a) SEM, b) TEM images, c) TG/DSC spectra of the $[Fe(BTO)(H_2O)_2]_n$/GO composites and d) FT-IR spectrum of the gas products. e) Infrared images and f) Infrared temperature measurement of the $[Fe(BTO)(H_2O)_2]_n$/GO deflagration process. (A colour version of this figure can be viewed online.)

To investigate the EMOFs deflagration advantages on the morphology and structure of the obtained Fe_3O_4/RGO samples, transmission electron microscope (TEM) characterization was conducted. TEM images of Fe_3O_4/RGO-3 sample synthesized from deflagration of $[Fe(BTO)(H_2O)_2]_n$/GO were shown in Fig. 4a–c, from which it can be observed that a large quantity of small spherical Fe_3O_4 nanoparticles were well decorated on two-dimensional RGO sheets. The large Fe_3O_4 nanoparticles were formed by the aggregation of small ones with the size of about 10 nm (as shown in the insert of Fig. 4b). The average size of the Fe_3O_4 nanoparticles was estimate to be about 10 nm (Figure S4). And all the obtained Fe_3O_4 nanoparticles exhibited high crystallinity degree with an exposed (311) facet (0.25 nm in d-spacing), suggesting the advantages of EMOFs-deflagration induced high local temperature on the small crystal growth. It should be noted that both sides of the RGO nanosheets were decorated with Fe_3O_4 nanoparticles uniformly (Figure S5). And, no individual Fe_3O_4 nanoparticles can be observed after sonication, indicating the strong interaction between Fe_3O_4 and RGO. That may be resulted from the high impacting effect of EMOFs-deflagration generated Fe species, which sprayed from the EMOFs to their surroundings and smashed into graphene oxide, resulting in a very close distance and a strong van der Waals

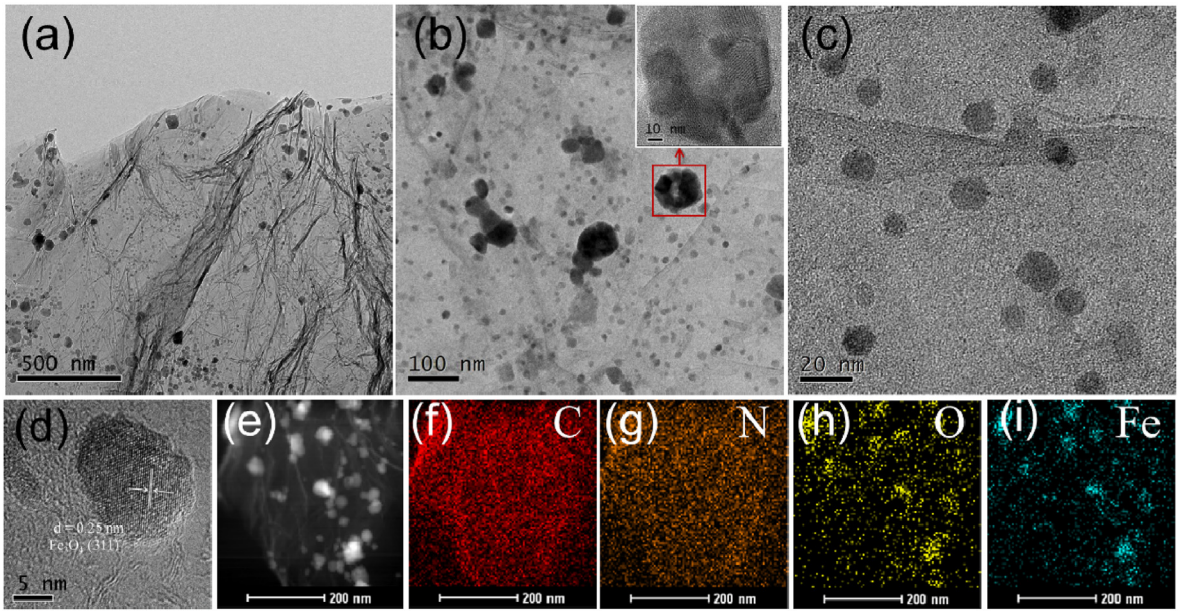

Fig. 4. a-e) TEM images and f-i) the element mappings of Fe_3O_4/RGO-3 sample. (A colour version of this figure can be viewed online.)

interaction between the final Fe_3O_4 nanoparticles and RGO products. Additionally, it's found that Fe_3O_4 nanoparticles from $[Fe(BTO)(H_2O)_2]_n$ deflagration tend to aggregate into large particles (Figure S6, Supporting Information), suggesting the important support role of RGO to prevent the agglomeration of Fe_3O_4 nanoparticles. The uniformly decorated Fe_3O_4 ultra-small nanoparticles and their strong interaction with RGO led to the formation of abundant Fe_3O_4/RGO interfaces with sufficient contact, which could greatly improve the interfacial polarization and the final microwave absorption performance of Fe_3O_4/RGO samples.

From the electron energy loss spectroscopy (EELS) elemental mappings in Fig. 4f–j, it can be observed that C and N species are homogeneously distributed within the RGO nanosheet, indicating that RGO was doped with N in the deflagration process utilizing the N-contained radicals as N source. However, Fe and O distributed not only within the Fe_3O_4 nanoparticles as observed in Fig. 4e, but also in the rest areas of RGO, suggesting the existence of plentiful ultra-small Fe_3O_4 nanoparticles. In addition, it can be observed that the O mapping shows some heterogeneous distribution and is much less abundant than the C and N mappings, indicating that the O element signals root mainly from Fe_3O_4 nanoparticles but not RGO, which further demonstrating the effectively reduction effect of EMOFs on GO.

To confirm the effect of $[Fe(BTO)(H_2O)_2]_n$ deflagration on the RGO reduction in the obtained Fe_3O_4/RGO samples, X-ray diffraction (XRD), Raman spectroscopy, Fourier-transform Infrared spectroscopy (FT-IR) and X-ray photoelectron spectroscopy (XPS) were performed.

The XRD patterns of pristine GO nanosheets and Fe_3O_4/RGO nanocomposites prepared by $[Fe(BTO)(H_2O)_2]$ deflagration treatment are shown in Fig. 5a. The diffraction peaks at 30.2°, 35.6°, 43.2°, 57.1° and 62.7° are indexed to the (220), (311), (400), (511) and (440) planes of Fe_3O_4 (JCPDS Card 89–3854), respectively [33]. The Fe_3O_4/RGO samples synthesized from different amounts of EMOFs deflagration treatments show the same XRD pattern except for the gradually enhanced diffraction peaks of Fe_3O_4, which may be resulted from the increased contents of Fe_3O_4. The mass percentages of Fe_3O_4 in Fe_3O_4/RGO samples were calculated to be ca. 12.2%, 23.2%, 33.6% and 42.1% for Fe_3O_4/RGO-1, Fe_3O_4/RGO-2, Fe_3O_4/RGO-3 and Fe_3O_4/RGO-4 samples, respectively (Table S1).

In order to obtain further information of Fe_3O_4/RGO samples, Raman spectroscopy was carried out to characterize the structural change of GO during the EMOFs deflagration treatment process. From the Raman spctra in Fig. 5b, two Raman peaks at 1350 and 1593 cm^{-1} can be observed in pristine GO sample, which corresponding to the D and G band, respectively. After treated by $[Fe(BTO)(H_2O)_2]_n$ deflagration, nearly all Fe_3O_4/RGO samples show the same Raman peaks. However, the D/G intensity ratios (I_D/I_G) are 0.90 for GO, 0.87 for Fe_3O_4/RGO-1, 0.90 for Fe_3O_4/RGO-2, 0.92 for Fe_3O_4/RGO-3 and 0.97 for Fe_3O_4/RGO-4, respectively. It can be inferred from the change in I_D/I_G that more numerous sp^2 domains in the carbon were achieved firstly, resulted from the deflagration-induced reduction of GO. However, with the addition of more EMOFs for deflagration, the sp^3 domains in carbon obviously increased due to the improved N doping levels (Table S2).

FT-IR was adopted to show the changes of organic groups of GO before and after the deflagration, as shown in Fig. 5c. The pristine GO shows rich functional groups including C═O, C═C, *O*–H, C–OH and C–O with the responding FT-IR absorption bands at 1734, 1624, 1374, 1227 and 1100 cm^{-1}, respectively [34]. The absorption bands at 3442 cm^{-1} were attributed to the vibrations of *O*–H from absorbed H_2O. Compared to the FT-IR curve of GO, only C═C and C–O bands can be observed in the FT-IR spectrum of Fe_3O_4/RGO, demonstrating the well reduction of GO via EMOFs deflagration. Especially, the C–O bands intensity decreased from Fe_3O_4/RGO-1 to Fe_3O_4/RGO-4, indicating the enhanced reduction effect of EMOFs on GO with more EMOFs added.

To get further information of RGO in the obtained Fe_3O_4/RGO samples, XPS was adopted to investigate the doping situation and chemical compositions of the Fe_3O_4/RGO samples. As shown in Fig. 5d, it can be observed that C 1s XPS spectra of Fe_3O_4/RGO series samples show the similar patterns but much difference from that of GO, indicating the removal of functional groups. O 1s XPs spectra were shown in Fig. 5f and consisted of four deconvoluted peaks that corresponding to *O*–H (533.5 eV), *O*–C═O (532.7 eV), C═O (531.5 eV) and Fe–O (530.1 eV), respectively [35]. Compared with pristine GO, it can be obviously observed that Fe_3O_4/RGO series samples showed gradually decreased *O*–H, *O*–C═O and C═O

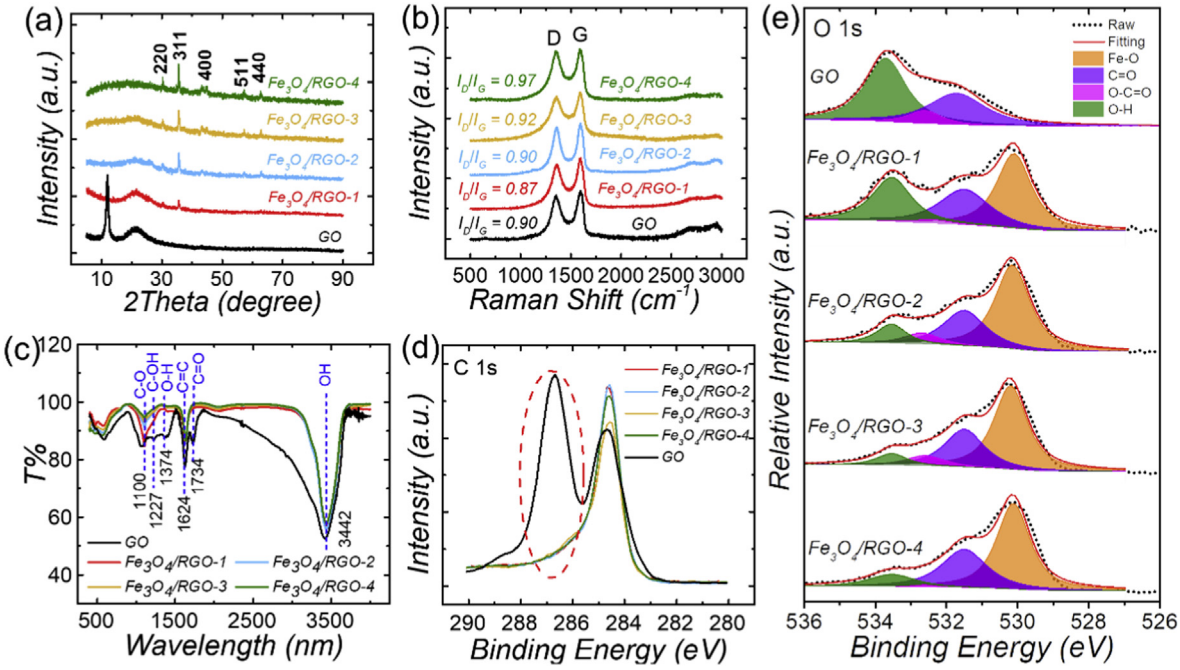

Fig. 5. a) XRD, b) Raman, c) FT-IR spectrum, d) C 1s and e) O 1s XPS spectra of GO and the obtained Fe_3O_4/RGO samples.

peaks with the increased amounts of EMOFs addition, which is in accordance with the FT-IR results. An interesting founding is that a slow spontaneous combustion phenomenon of the product can be observed with the color turning from black to red (Figure S7) when excess EMOFs deflagrated, suggesting that pure Fe nanoparticles existed as the mid product of EMOFs deflagration (Figure S8) and the O elements in Fe_3O_4 were partly from the oxygen-contained functional groups of graphene oxide. Additionally, from the full XPS spectra in Figure S9, only C, N, Fe and O elements can be observed, revealing the advantages in purity of [Fe(BTO)$(H_2O)_2$] deflagration method.

As depicted in Figure S10, when very small amount of [Fe(BTO)$(H_2O)_2$] was added, very few ultra-small Fe_3O_4 nanoparticles were produced and loaded on the RGO nanosheets in Fe_3O_4/RGO-1 sample. No aggregations can be observed but very few Fe_3O_4/RGO interfaces were formed. When increased the adding amount of EMOFs, the loading density of Fe_3O_4 nanoparticles was improved in Fe_3O_4/RGO-2 sample (Figure S11), indicating the growing Fe_3O_4/RGO interface numbers. However, slight aggregation phenomenon came up. When excess EMOFs were added, serious aggregation of Fe_3O_4 nanoparticles occurred and led to the decrease of Fe_3O_4/RGO interface numbers as shown in Figure S12. Among the Fe_3O_4/RGO series samples, Fe_3O_4/RGO-3 sample possess the most abundant Fe_3O_4 nanoparticles loading and Fe_3O_4/RGO interfaces. The abundant Fe_3O_4/RGO interfaces and highly reduced GO in Fe_3O_4/RGO series samples synthesized via our designed EMOFs deflagration method may exhibit excellent EM absorption performances.

To explore the EM wave absorption performances of Fe_3O_4/RGO samples, different contents of the products were mixed with paraffin to form composites by a simple blending method [36]. Based on the measured electromagnetic parameters, the *RL* values of Fe_3O_4/RGO/paraffin composites can be calculated under the transmission line theory:

$$RL = 20\log|(Z_m - Z_o)/(Z_m + Z_o)| \quad (1)$$

$$Z_{in} = Z_o\sqrt{\frac{\mu_r}{\varepsilon_r}}\tanh\left(j\frac{2\pi fd}{c}\sqrt{\mu_r\varepsilon_r}\right) \quad (2)$$

where Z_{in} is the input characteristic impedance, ε_r and μ_r are the complex permittivity and complex permeability, respectively; d is the absorber thickness, f is the frequency; and c is the velocity of light in free space. Fig. 6a–d shows the three-dimensional presentations of calculated theoretical *RL* values of four Fe_3O_4/RGO samples with different thickness (1–5 mm) in 2–18 GHz. It is notable that the microwave absorption performances vary a lot with the variation of Fe_3O_4 contents. In contrast, both the RL_{min} value and the effective absorption bandwidth (EAB) of Fe_3O_4/RGO-3 sample are larger and broader than the other three samples. The microwave absorption behaviors at low thickness (<2.0 mm) are rather good, with the *RL* values for all the measured thicknesses below −20 dB. The maximum EAB reaches 5.24 GHz at 1.8 mm, where the minimum RL value is −46.3 dB, and the minimum *RL* value reaches as strong as −67.1 dB at only 2.2 mm. It is worth mentioning that the loading content of Fe_3O_4/RGO sample in the Fe_3O_4/RGO/paraffin composites is merely 5 wt%. With the superior *RL* value and the broad EAB at low thickness with ultra-low filler loading, Fe_3O_4/RGO-3 sample exhibits great potential for application as high-efficiency microwave absorber.

In order to illuminate the microwave absorption mechanism of Fe_3O_4/RGO samples, the frequency dependence electromagnetic parameters are displayed in Fig. 7. As can be seen from Fig. 7a and b, the values of ε' and ε'' decrease with the increase of Fe_3O_4 loading, and evident frequency dispersion phenomena can be found in the tested frequency range. The dielectric values of Fe_3O_4/RGO-1 and Fe_3O_4/RGO-2 are higher than those of common dielectric materials, which is derived from the strong reduction effect of GO during deflagration. With the continued increase of Fe_3O_4 loading, the permittivity values (Fe_3O_4/RGO-3 and Fe_3O_4/RGO-4) gradually decrease. Enlarged curves were also plotted in the inset parts. No distinct resonance peak can be observed in the imaginary permittivity curves, indicating the conduction loss-dominated dielectric

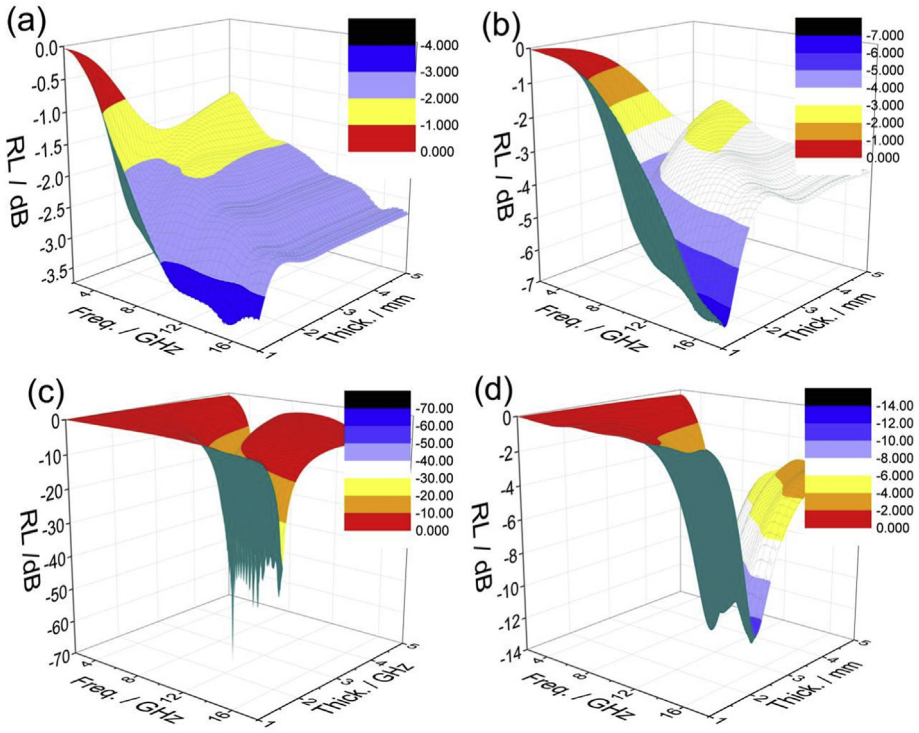

Fig. 6. 3D representations of the reflection loss (*RL*) of the obtained Fe_3O_4/RGO samples: a) Fe_3O_4/RGO-1, b) Fe_3O_4/RGO-2, c) Fe_3O_4/RGO-3 and d) Fe_3O_4/RGO-4. (A colour version of this figure can be viewed online.)

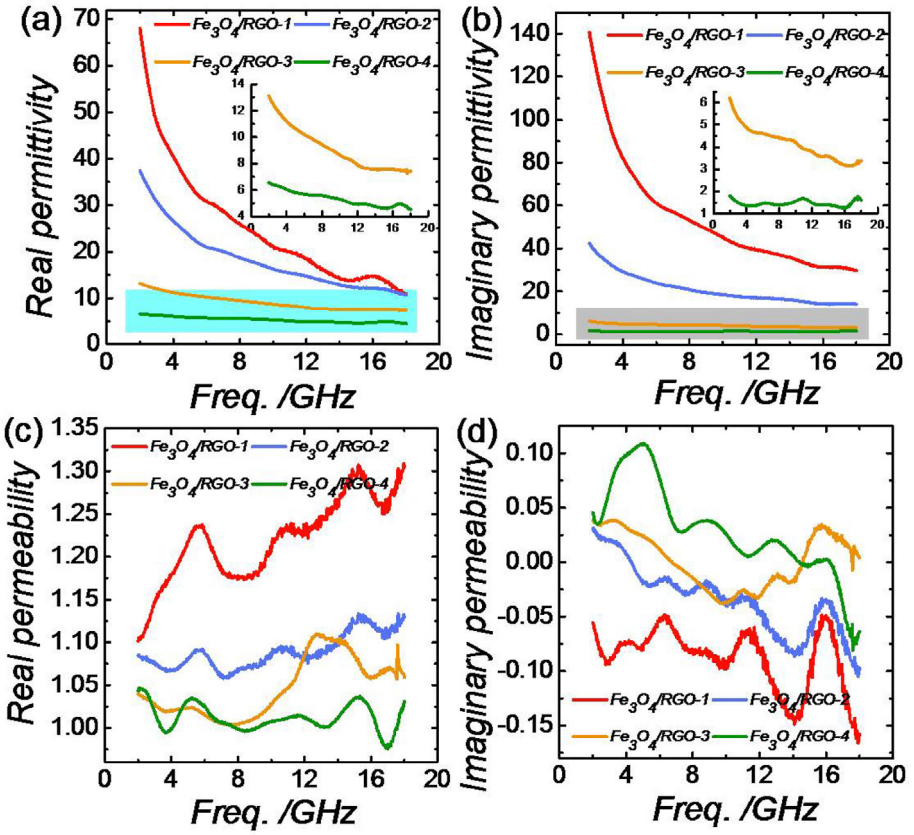

Fig. 7. The electromagnetic parameters of the obtained Fe_3O_4/RGO samples.

dissipation for Fe_3O_4/RGO samples. Permeability values of the four samples show little change from 1.0 to 1.35 (Fig. 7c and d). The relatively low permeability of Fe_3O_4/RGO composites is mainly derived from the following two reasons. One is that magnetic materials at nanoscale often possess weak permeability behaviors due to the nano-size effect. The second one is that the permeability values are the overall effect of the composites composed of Fe_3O_4 and RGO, not only Fe_3O_4 species. The obvious fluctuations in the curves are derived from the residual loss, including domain wall resonance, nature resonance, dimension resonance and exchange resonance. Generally, residual loss comes from the relaxation process during magnetization. The appeared resonance peaks at low frequency are derived from natural resonances, the resonances peaks at higher frequency mainly come from exchange resonances.

According to Debye theory, the complex permittivity can be expressed with the following equations:

$$\varepsilon' = \varepsilon_\infty + \frac{\varepsilon_s - \varepsilon_\infty}{1 + (2\pi f)^2 \tau^2} \tag{3}$$

$$\varepsilon'' = (\varepsilon_s - \varepsilon_\infty)\frac{2\pi f \tau}{1 + (2\pi f)^2 \tau^2} + \frac{\sigma}{2\pi f \varepsilon_0} \tag{4}$$

where ε_s is the static permittivity, ε_∞ is the relative dielectric permittivity at high-frequency limit, τ is the polarization relaxation time, σ is the electrical conductivity.

By subtracting the contribution of σ from equation (4) and eliminating $2\pi f\tau$ part, the relationship between ε' and ε'' would be a semicircle, namely the Cole-Cole semicircle. Each semicircle is corresponding to a single Debye relaxation process [37]. As can be seen in Fig. 8a and b, no evident semicircle but upward curves are found for sample Fe_3O_4/RGO-1 and Fe_3O_4/RGO-2, indicating their conduction loss dominated dielectric loss process. Obvious semicircles can be observed for both Fe_3O_4/RGO-3 and Fe_3O_4/RGO-4 (Fig. 8c and d). The more semicircles of Fe_3O_4/RGO-4 indicate its more dielectric polarization processes than those of Fe_3O_4/RGO-3. In consideration of the chemical compositions of these samples, we infer that the more dielectric polarization processes are derived from the enhanced MWS effect. In other words, more Fe_3O_4 particles induce more interfacial polarizations between the interfaces of Fe_3O_4 and RGO. In view of the relatively large permittivity values of Fe_3O_4/RGO samples, we suppose that polarization has less contribution to the dielectric loss. Based on equations (3) and (4), if ε'' is mainly derived from conductivity, it can be expressed as:

$$\varepsilon'' = \frac{\sigma}{2\pi f \varepsilon_0} \tag{5}$$

As can be seen, ε'' is proportional to *1/f*. We plotted the curves of ε'' verus *1/f* to detect the electrical conductivity differences between Fe_3O_4/RGO samples, where the slope $\sigma/(2\pi\varepsilon_0)$ of straight line stands for the conduction capability. As reflected in Fig. 8e–h, the electrical conductivity decreases dramatically from Fe_3O_4/RGO-1 to Fe_3O_4/RGO-4, which is in accordance with the permittivity values variation in Fig. 6 as well as the analysis in Fig. 8a–d. From the loss mechanism comparison between the four samples, it can be found that Fe_3O_4/RGO-3 sample, with the optimal microwave absorption performance, does not possess obvious dissipation advantages either in polarization or conduction loss.

Impedance matching was also explored based on the normalized impedance Z_{in}/Z_o. When the value equals to 1, the incident microwave can be fully absorbed [38]. Here, we detected the impedance matching characters for the four samples at some typical thicknesses, that is, 1.0 mm, 1.5 mm, 2.0 mm, 2.5 mm, 3.0 mm, 3.5 mm, 4.0 mm, 4.5 mm and 5.0 mm. As shown in Fig. 9a–d, the normalized impedance values increase gradually from Fe_3O_4/RGO-1 to Fe_3O_4/RGO-4. The values of Fe_3O_4/RGO-1 and Fe_3O_4/RGO-2 are too low, while that of Fe_3O_4/RGO-4 is too high, all of which are not ideal impedance matching. As comparison, the normalized impedance values of Fe_3O_4/RGO-3 at all measured thickness are close to 1.0, indicating the excellent ability to introducing microwaves.

Base on the above analysis, it is not hard to find out that the optimal microwave absorption performance of Fe_3O_4/RGO-3 is derived from both the impedance matching and microwave dissipation. The normalized impedance characters directly influence the microwave reflection on the surface; as for the microwave loss mechanisms, it has been demonstrated that conduction loss contributes more than dielectric polarization.

Interference absorption is another important mechanism in microwave absorption process besides the as-described loss-type absorption. It can often be expressed by the following equation [39].

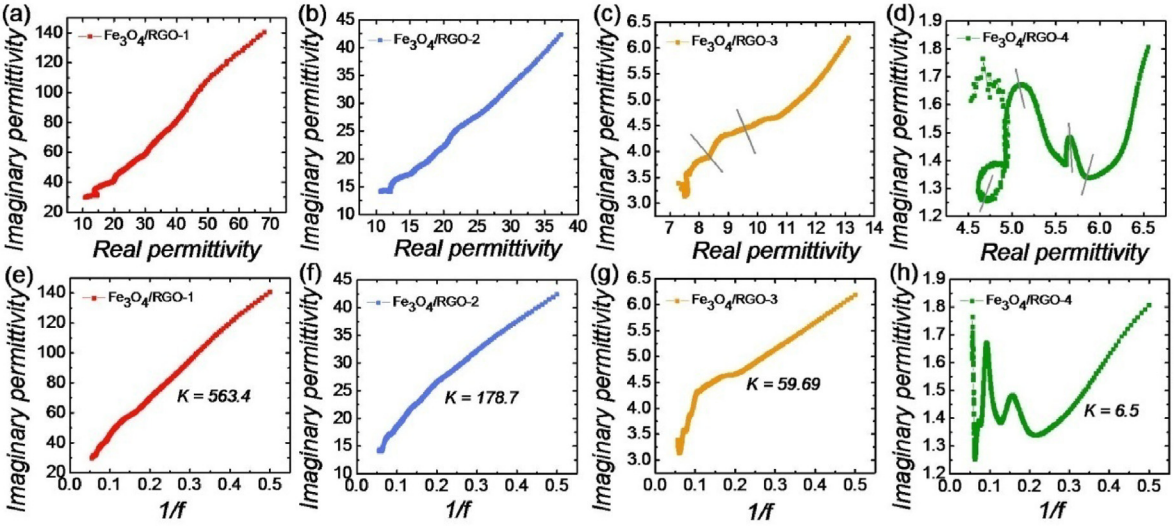

Fig. 8. Cole–Cole semicircles and ε''-f^{-1} curves of the obtained Fe_3O_4/RGO samples: a) and e) Fe_3O_4/RGO-1, b) and f) Fe_3O_4/RGO-2, c) and g) Fe_3O_4/RGO-3, d) and h) Fe_3O_4/RGO-4. (A colour version of this figure can be viewed online.)

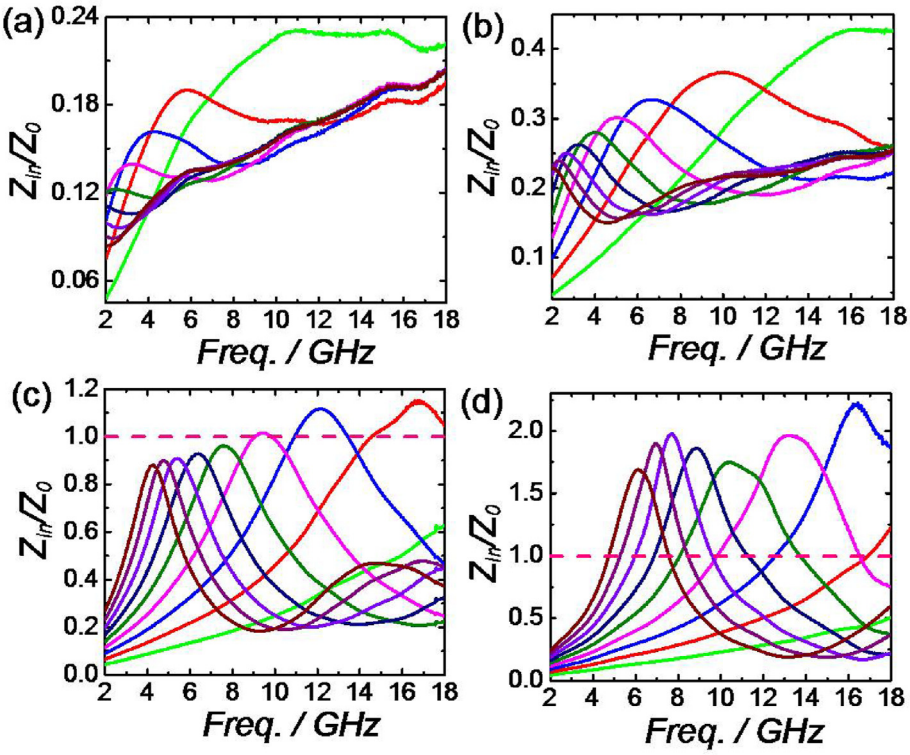

Fig. 9. Normalized input impedance Z_{in}/Z_o of a) Fe_3O_4/RGO-1, b) Fe_3O_4/RGO-2, c) Fe_3O_4/RGO-3 and d) Fe_3O_4/RGO-4 at different thicknesses (from right side to the left: 1.0–5.0 mm, interval is 0.5 mm).

$$t_m = nc \Big/ 4f\sqrt{|\mu_r||\varepsilon_r|}^{(n=1,3,5,\ldots)} \quad (6)$$

As seen from the equation, if the absorber thickness at peak frequency is equal to the calculated thickness t_m, the incident microwaves and reflected waves would meet face to face (out of 180°), resulting in the disappearance of each other at the air-absorber interfaces. As reflected in Fig. 10, all the detected thicknesses at peak frequency are in accordance with the $\lambda/4$, which demonstrates that the geometrical effect (interference absorption) also acts as a critical role in the enhanced microwave absorption, especially for the maximum reflection loss values.

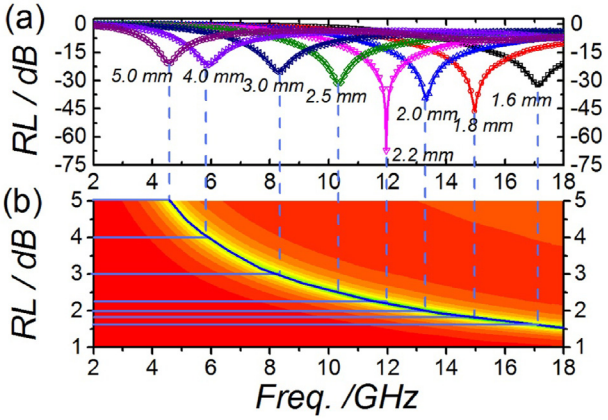

Fig. 10. Frequency dependence of reflection loss of Fe_3O_4/RGO-3 (a) and 2D contour of RL curves and calculated thickness based on λ/4 models of Fe_3O_4/RGO-3 (b). (A colour version of this figure can be viewed online.)

3. Conclusion

In summary, we have developed a novel EMOFs deflagration methodology to prepare magnetic/dielectric nanocomposite absorbers. In the employed case, $[Fe(BTO)(H_2O)_2]_n$ was used as the EMOF precursor, which can be initiated at a low temperature (ca. 220 °C) and finished in seconds, showing prominent advantages of energy- and time-saving. The spray behavior of Fe species and huge heat release in the deflagration process lead to the formation of ultra-small Fe_3O_4 nanoparticles and fast reduction of GO, respectively. The loading amount of Fe_3O_4 ultra-small nanoparticles and the reduction level of GO can be regulated by controlling the adding amount of EMOFs, which influences the electromagnetic parameters of Fe_3O_4 and RGO as well as the final performances. An optimal sample, Fe_3O_4/RGO-3, shows a minimum *RL* of −67.1 dB at only 2.2 mm with merely 5 wt% of sample loading. This work proposes a novel EMOF deflagration methodology to synthesize electromagnetic absorption materials, and underpin the future research efforts to develop other advanced materials.

4. Experimental section

Synthesis of $[Fe(BTO)(H_2O)_2]_n$: 1.13g (4 mmol) $FeSO_4 \bullet 7H_2O$ and 0.094 g BTO (4 mmol) was added to 20 mL water with constant stirring, respectively. Then, the BTO Solution was added to $FeSO_4$ solution dropwise under stirring, resulting the formation of a beige suspension. After stirring for 30 min at room temperature, the $[Fe(BTO)(H_2O)_2]_n$ were obtained after centrifuged for three times, washed with deionized water and dried in a vacuum oven at 60 °C for 12 h.

Synthesis of $[Fe(BTO)(H_2O)_2]n$/GO: 10 g graphene oxide solution (11 mg/g) was added to 200 mL water and stirred for 15 min to obtain a homogeneous GO dilute solution. Then, a 20 mL solution

containing x mmol $FeSO_4 \bullet 7H_2O$ was firstly added to GO solution under stirring for 15 min to achieve the adsorption of Fe^{2+} on the GO surfaces. After that, the solution containing x mmol BTO were dropwise added into the above solution and stirred for 30 min, resulting the formation of a grey suspension. $[Fe(BTO)(H_2O)_2]_n$/GO were then obtained after the precipitate was centrifuged for three times, washed with deionized water and then dried in a vacuum oven at 60 °C for 12 h.

Synthesis of Fe_3O_4/RGO: The as-prepared $[Fe(BTO)(H_2O)_2]_n$/GO were placed in a high-pressure reactor (MS100-P8-T3-HC1-SV, Anhui Kemi machinery technology Co. LTD) and heated to 220 °C quickly at certain heating rate to trigger the $[Fe(BTO)(H_2O)_2]_n$ deflagration. Herein, the high-pressure reactor was used to protect the final products from oxidation by oxygen in air at high temperature and aviod potential danger from the ultra-fast exergonic deflagration process. Once ignited, the energetic $[Fe(BTO)(H_2O)_2]_n$ MOFs will undergo substantially rapid, self-propagating reactions, generate various radicals and gas products, and liberate heat in less than 1 s, which lead to the formation of a high-temperature and -pressure environment. When a jump of the pressure meter indicator was observed, turn off the heating power and cool the reactor to room temperature naturally. After the pressure is released, the products were then collected and washed with deionized water for three times. After dried in a vacuum oven at 60 °C for 12 h, the final Fe_3O_4/RGO were then obtained and labeled as Fe_3O_4/RGO-x (where x represents the adding amount BTO, x mmol).

Characterization: The crystal structures, morphologies and particle sizes of the sample were examined via X-ray diffraction (XRD, D8 advance, Bruker), Field emission scanning electron microscopy (FESEM, Sigma-HD, Zeiss), transmission electron microscopy (TEM JEM-2100F, JEOL), respectively. The thermal decomposition characteristics and gas products of EMOFs were determined via a thermogravimetric and differential scanning calorimetry (TGA-DSC, NETZSCH 209F3) equipped with an FT-IR spectrometer (Bruker Tensor 27). The FT-IR spectra of the functional groups in GO and Fe_3O_4/RGO samples were obtained using a FT-IR spectrometer (Agilent Cary 660). The chemical compositions of the samples were investigated via an ESCALAB 250 XPS X-ray Electron Spectrometer (American Thermo Electron Corporation).

Properties: Electromagnetic parameters including complex permittivity and permeability were investigated with a vector network analyzer (Agilent, N5244A) at the frequency range of 2–18 GHz. The Fe_3O_4/RGO samples were dispersed in paraffin wax with a mass ratio of 5 wt% and put into a metal mold (inner/outer diameter: and 3.0/7.0 mm) and pressed into a ring with a thickness of about 2.25 mm. The RL values were calculated using the measured complex permittivity and permeability.

Declaration of competing interest

The authors declare that they have no known competing financial interests or personal relationships that could have appeared to influence the work reported in this paper.

CRediT authorship contribution statement

Yousong Liu: Writing - original draft. **Bin Quan:** Formal analysis. **Xiaohui Liang:** Formal analysis. **Bing Huang:** Resources. **Shiliang Huang:** Formal analysis. **Xiaodong Li:** Formal analysis. **Guangbin Ji:** Formal analysis. **Zhong Jin:** Writing - original draft. **Guangcheng Yang:** Writing - original draft.

Acknowledgements

This work was supported by the National Natural Science Foundation of China (Nos. 11702264, 11702268, 21703217, 11772307, 11802276, 21872069', 51761135104 and 21573108), National Key R&D Program of China (2017YFA0208200, 2016YFB0700600, 2015CB659300), Natural Science Foundation of Jiangsu Province (BK20180008), and the Fundamental Research Funds for the Central Universities.

Appendix A. Supplementary data

Supplementary data related to this article can be found at https://doi.org/10.1016/j.carbon.2020.04.089.

References

[1] J. Feng, Y. Hou, Y. Wang, L. Li, Synthesis of hierarchical $ZnFe_2O_4$@SiO_2@RGO core-shell microspheres for enhanced electromagnetic wave absorption, ACS Appl. Mater. Interfaces 9 (2017) 14103–14111.
[2] H.L. Lv, Z.H. Yang, H.B. Xu, L.Y. Wang, R.B. Wu, An electrical switch-driven flexible electromagnetic absorber, Adv. Funct. Mater. 30 (2020) 1907251.
[3] H. Lv, Z. Yang, S.J.H. Ong, C. Wei, H. Liao, S. Xi, et al., A flexible microwave shield with tunable frequency transmission and electromagnetic compatibility, Adv. Funct. Mater. 29 (2019) 1900163.
[4] Q.W. Wang, H.B. Zhang, J. Liu, S. Zhao, X. Xie, L. Liu, et al., Multifunctional and water-resistant MXene-decorated polyester textiles with outstanding electromagnetic interference shielding and joule heating performances, Adv. Funct. Mater. 29 (2019) 1806819.
[5] Y. Zhang, P. Wang, Y. Wang, L. Qiao, T. Wang, F. Li, Synthesis and excellent electromagnetic wave absorption properties of parallel aligned FeCo@C core–shell nanoflake composites, J. Mater. Chem. C 3 (2015) 10813–10818.
[6] S. Zhao, H.B. Zhang, J.Q. Luo, Q.W. Wang, B. Xu, S. Hong, et al., Highly electrically conductive three-dimensional $Ti_3C_2T_x$ MXene/reduced graphene oxide hybrid aerogels with excellent electromagnetic interference shielding performances, ACS Nano 12 (2018) 11193–11202.
[7] J. Liu, H.B. Zhang, X. Xie, R. Yang, Z. Liu, Y. Liu, et al., Multifunctional, superelastic, and lightweight MXene/polyimide aerogels, Small 14 (2018) 1802479.
[8] W.L. Song, X.T. Guan, L.Z. Fan, Y.B. Zhao, W.Q. Cao, C.Y. Wang, et al., Strong and thermostable polymeric graphene/silica textile for lightweight practical microwave absorption composites, Carbon 100 (2016), 109–17.
[9] L. Zhu, X. Zeng, X. Li, B. Yang, R. Yu, Hydrothermal synthesis of magnetic Fe_3O_4/graphene composites with good electromagnetic microwave absorbing performances, J. Magn. Magn Mater. 426 (2017) 114–120.
[10] J. Liu, M.S. Cao, Q. Luo, H.L. Shi, W.Z. Wang, J. Yuan, Electromagnetic property and tunable microwave absorption of 3D nets from nickel chains at elevated temperature, ACS Appl. Mater. Interfaces 8 (2016) 22615–22622.
[11] F. Meng, H. Wang, F. Huang, Y. Guo, Z. Wang, D. Hui, et al., Graphene-based microwave absorbing composites: a review and prospective, Compos. B Eng. 137 (2018) 260–277.
[12] T. Wu, Y. Liu, X. Zeng, T. Cui, Y. Zhao, Y. Li, et al., Facile hydrothermal synthesis of Fe_3O_4/C core–shell nanorings for efficient low-frequency microwave absorption, ACS Appl. Mater. Interfaces 8 (2016) 7370–7380.
[13] N. Li, G.W. Huang, Y.Q. Li, H.M. Xiao, Q.P. Feng, N. Hu, et al., Enhanced microwave absorption performance of coated carbon nanotubes by optimizing the Fe_3O_4 nanocoating structure, ACS Appl. Mater. Interfaces 9 (2017) 2973–2983.
[14] C. Zhang, B. Wang, J. Xiang, C. Su, C. Mu, F. Wen, et al., Microwave absorption properties of CoS_2 nanocrystals embedded into reduced graphene oxide, ACS Appl. Mater. Interfaces 9 (2017) 28868–28875.
[15] Q. Li, J. Liu, Y. Zhao, X. Zhao, W. You, X. Li, et al., "Matryoshka doll"-like CeO_2 microspheres with hierarchical structure to achieve significantly enhanced microwave absorption performance, ACS Appl. Mater. Interfaces 10 (2018) 27540–27547.
[16] H.B. Zhao, J.B. Cheng, J.Y. Zhu, Y.Z. Wang, Ultralight CoNi/rGO aerogels toward excellent microwave absorption at ultrathin thickness, J. Mater. Chem. C 7 (2019) 441–448.
[17] H. Lv, Z. Yang, P.L. Wang, G. Ji, J. Song, L. Zheng, et al., A voltage-boosting strategy enabling a low-frequency, flexible electromagnetic wave absorption device, Adv. Mater. 30 (2018) 1706343.
[18] C. Chen, J. Xi, E. Zhou, L. Peng, Z. Chen, C. Gao, Porous graphene microflowers for high-performance microwave absorption, Nano-Micro Lett. 10 (2017) 26.
[19] Z. Li, X. Han, Y. Ma, D. Liu, Y. Wang, P. Xu, et al., MOFs-derived hollow Co/C microspheres with enhanced microwave absorption performance, ACS Sustain. Chem. Eng. 6 (2018) 8904–8913.
[20] J. Tang, R.R. Salunkhe, J. Liu, N.L. Torad, M. Imura, S. Furukawa, et al., Thermal conversion of core–shell metal–organic frameworks: a new method for selectively functionalized nanoporous hybrid carbon, J. Am. Chem. Soc. 137 (2015) 1572–1580.
[21] W. Liu, L. Liu, G. Ji, D. Li, Y. Zhang, J. Ma, et al., Composition design and structural characterization of MOF-derived composites with controllable electromagnetic properties, ACS Sustain. Chem. Eng. 5 (2017) 7961–7971.

[22] W. Liu, J. Liu, Z. Yang, G. Ji, Extended working frequency of ferrites by synergistic attenuation through a controllable carbothermal route based on prussian blue shell, ACS Appl. Mater. Interfaces 10 (2018) 28887–28897.
[23] Z. Deng, Y. Li, H.B. Zhang, Y. Zhang, J.Q. Luo, L.X. Liu, et al., Lightweight Fe@C hollow microspheres with tunable cavity for broadband microwave absorption, Composites Part B 177 (2019) 107346.
[24] X.P. Liu, Z. Deng, Y. Li, H.B. Zhang, S. Zhao, Y. Zhang, et al., Controllable synthesis of hollow microspheres with Fe@Carbon dual-shells for broad bandwidth microwave absorption, Carbon 147 (2019) 172–181.
[25] X. Chen, F. Meng, Z. Zhou, X. Tian, L. Shan, S. Zhu, et al., One-step synthesis of graphene/polyaniline hybrids by in situ intercalation polymerization and their electromagnetic properties, Nanoscale 6 (2014) 8140–8148.
[26] X. Jian, X. Xiao, L. Deng, W. Tian, X. Wang, N. Mahmood, et al., Heterostructured nanorings of Fe–Fe_3O_4@C hybrid with enhanced microwave absorption performance, ACS Appl. Mater. Interfaces 10 (2018) 9369–9378.
[27] G. Wang, Z. Gao, S. Tang, C. Chen, F. Duan, S. Zhao, et al., Microwave absorption properties of carbon nanocoils coated with highly controlled magnetic materials by atomic layer deposition, ACS Nano 6 (2012) 11009–11017.
[28] G. Yang, X. Li, EM-to-AM:A strategy for construction of advanced materials using energy-releasing effect of energetic materials, Chin. J. Energetic Mater. 26 (2018) 1000–1002.
[29] Y. Liu, B. Gao, Z. Qiao, Y. Hu, W. Zheng, L. Zhang, et al., Gram-scale synthesis of graphene quantum dots from single carbon atoms growth via energetic, Material Deflagration. Chem. Mater. 27 (2015) 4319–4327.
[30] Y. Liu, S. Ouyang, W. Guo, H. Zong, X. Cui, Z. Jin, et al., Ultrafast one-step synthesis of N and Ti^{3+} codoped TiO_2 nanosheets via energetic material deflagration, Nano Res 11 (2018) 4735–4743.
[31] Y. Liu, B. Huang, S. Peng, T. Wang, G. Ji, G. Yang, et al., Deflagration synthesis of nitrogen/fluorine co-doped hollow carbon nanoparticles with excellent oxygen reduction performance, Inorg. Chem. Front. 5 (2018) 1307–1313.
[32] R. Zhao, Z. Liang, S. Gao, C. Yang, B. Zhu, J. Zhao, et al., Puffing up energetic metal–organic frameworks to large carbon networks with hierarchical porosity and atomically dispersed metal sites, Angew. Chem. Int. Ed. 58 (2019) 1975–1979.
[33] J. Yu, F. Chi, Y. Sun, J. Guo, X. Liu, Assembled porous Fe_3O_4@g-C_3N_4 hybrid nanocomposites with multiple interface polarization for stable microwave absorption, Ceram. Int. 44 (2018) 19207–19216.
[34] Q. Guan, J. Cheng, B. Wang, W. Ni, G. Gu, X. Li, et al., Needle-like Co_3O_4 anchored on the graphene with enhanced electrochemical performance for aqueous supercapacitors, ACS Appl. Mater. Interfaces 6 (2014) 7626–7632.
[35] S. Venkateswarlu, D. Lee, M. Yoon, Bioinspired 2D-carbon flakes and Fe_3O_4 nanoparticles composite for arsenite removal, ACS Appl. Mater. Interfaces 8 (2016) 23876–23885.
[36] X.J. Zhang, S. Li, S.W. Wang, Z.J. Yin, J.Q. Zhu, A.P. Guo, et al., Self-supported construction of three-dimensional MoS_2 hierarchical nanospheres with tunable high-performance microwave absorption in broadband, J. Phys. Chem. C 120 (2016) 22019–22027.
[37] X.J. Zhang, J.Q. Zhu, P.G. Yin, A.P. Guo, A.P. Huang, L. Guo, et al., Tunable high-performance microwave absorption of $Co_{1-x}S$ hollow spheres constructed by nanosheets within ultralow filler loading, Adv. Funct. Mater. 28 (2018) 1800761.
[38] Y. Zhang, H.B. Zhang, X. Wu, Z. Deng, E. Zhou, Z.Z. Yu, Nanolayered Cobalt@Carbon hybrids derived from metal–organic frameworks for microwave absorption, ACS Appl. Nano Mater. 2 (2019) 2325–2335.
[39] B. Quan, X. Liang, X. Zhang, G. Xu, G. Ji, Y. Du, Functionalized carbon nanofibers enabling stable and flexible absorbers with effective microwave response at low thickness, ACS Appl. Mater. Interfaces 10 (2018) 41535–41543.